Thermal stability of hierarchical microstructural features in additively manufactured stainless steel

Funch, Cecilie V; Grumsen, Flemming B; da Silva Fanta, Alice B; Christiansen, Thomas L; Somers, Marcel A J

Published in:
Heliyon

Link to article, DOI:
10.1016/j.heliyon.2023.e16555

Publication date:
2023

Document Version
Publisher's PDF, also known as Version of record

Heliyon 9 (2023) e16555

Contents lists available at ScienceDirect

Heliyon

journal homepage: www.cell.com/heliyon

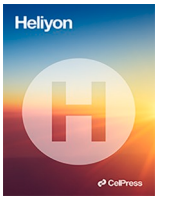

Research article

Thermal stability of hierarchical microstructural features in additively manufactured stainless steel

Cecilie V. Funch [a,1,*], Flemming B. Grumsen [a], Alice B. da Silva Fanta [b], Thomas L. Christiansen [a], Marcel A.J. Somers [a]

[a] *Department of Civil and Mechanical Engineering, Technical University of Denmark, Produktionstorvet, Building 425, 2800 Kongens Lyngby, Denmark*

[b] *National Centre for Nanofabrication and Characterization, Technical University of Denmark, Oersteds Plads, Building 347, 2800 Kongens Lyngby, Denmark*

ARTICLE INFO

Keywords:
Austenitic stainless steel
Additive manufacturing
Hierarchical microstructure
Thermal stability

ABSTRACT

Additive manufacturing of austenitic stainless steel results in an unconventional hierarchical microstructure. This hierarchical microstructure was investigated in detail in the as-built condition. The hierarchical microstructure consists of elongated austenite grains and melt pool fusion boundaries with a spherical cap morphology at the largest length scale. At a smaller length scale elongated columnar cell structures exist with elemental segregation at the cell walls. The cells were found not to be a misorientation structure in themselves as often noted, but rather groups of cells with a specific orientation, which are collected in 3–5 μm domains. At even smaller length scales, amorphous spherical silicates are found along with a high dislocation density along cell walls. The thermal stability of the unconventional features as melt pool boundaries, elongated austenite grains, cell domains, cell structure, amorphous precipitates was investigated systematically in the temperature range 400–1100 °C. The dislocation network forming the cell boundaries dissolves gradually and remains thermally stable up to about 800 °C. The melt pool boundaries are more thermally stable and dissolve above 900 °C. The elongated austenite grains and crystallographic texture are fully stable within the investigated temperature range. The cell domains appear to be pinned by precipitation as the cellular structure is dissolved and gradually straighten and resemble regular low angle grain boundaries. The amorphous silicates act as heterogeneous nucleation sites for the formation of σ-phase in the temperature range 700–800 °C, while at higher treatment temperatures these silicates are replaced by large, oblong Si–Mn oxides and small, round Mn–Cr oxides.

1. Introduction

Austenitic stainless steel AISI 316 L is a widely applied engineering alloy due to its excellent corrosion resistance in combination with good mechanical and deformation properties. Its widespread industrial application and a cooling behaviour (virtually) free of martensitic transformation have made AISI 316 L one of the most commonly adopted alloys in additive manufacturing (AM). Metal

* Corresponding author.
E-mail address: cecilie.funch@sydney.edu.au (C.V. Funch).
[1] Now with: Sydney Manufacturing Hub, The University of Sydney, Camperdown, NSW 2006, Australia.

https://doi.org/10.1016/j.heliyon.2023.e16555
Received 24 March 2023; Received in revised form 17 May 2023; Accepted 19 May 2023
Available online 23 May 2023

additive manufacturing (MAM) has gained increasing interest from industrial perspectives as the process reliability, speed and part quality have improved steadily, particularly in the last 5–10 years. Several MAM processes have been proposed for the fabrication of austenitic stainless steels. Among those, laser powder-bed fusion (L-PBF) is one of the most prominent processes, because it provides a good compromise of cost, process speed and part density [1]. In the L-PBF process, a thin layer of gas-atomized powder is spread over the build platform and a high-power laser is rastered over the surface. Locally, the temperature is raised above the melting point of the material. By rapidly moving the laser over the powder bed, the material is therefore selectively melted and solidified (fused) at the desired locations. After finishing the fusion at all pre-selected locations in the deposited layer, the build plate is lowered, a new layer of powder is spread and the process is repeated until the final part geometry is achieved [1,2]. The main benefits of additive manufacturing over conventional manufacturing (subtractive machining, forging, casting etc.) include geometrical freedom, full customization of component designs, near net shape manufacturing, low batch production capabilities and unique microstructures and properties. In L-PBF, the rapid movement of the laser (and thereby the melt pool) creates steep thermal gradients as well as high solidification rates. These characteristics of the L-PBF process result in non-equilibrium microstructures, unachievable by conventional manufacturing methods. In the case of austenitic stainless steel 316 L, the L-PBF process results in a hierarchical microstructure consisting of austenite grains, elongated in the build direction, which contain a cellular structure. The walls of the cells usually have a higher content of ferrite-forming alloying elements, in particular chromium and molybdenum, and have a high dislocation density and dislocation tangles along the cell boundaries. The origin of this cellular structure and dislocation structures is still unclear, and several hypotheses have been put forward to explain these features. For example constitutional super-cooling, interface stability theories as well as a strong vortex flow caused by Marangoni convection have been suggested [3–5]. Other hypotheses include residual stresses formed during solidification, causing intrinsic strain ageing during the processing of subsequent layers [6]. At a macro-scale level, fusion boundaries, also referred to as melt pool boundaries, are observed, which have a spherical cap morphology and their size depends on the applied laser parameters. Furthermore, amorphous nano-scale silicates are formed during L-PBF of 316 L due to the presence of residual oxygen in the build chamber and/or powder [5]. The composition of these nano-scale silicates is not entirely clear, but they may contain transition-metal alloying elements [3,7–9].

Heat treatment of L-PBF 316 L at a variety of temperatures and treatment times has been investigated, particularly at relatively high temperatures where recrystallization and solution annealing are anticipated to occur. The most common observation is related to the disappearance of the cellular structure by the dissolution of the dislocation network. This cell dissolution is observed to occur in the temperature range 800–900 °C [7,9–12]. The dislocation density can be reduced by recovery at temperatures, where the cellular structure itself does not yet dissolve [10]. Furthermore, some coarsening of the cell structure was observed prior to dissolution during extended treatment times [11,13]. Deng et al. found that while some cellular coarsening occurred, the cellular structure of AM 316 L was much more stable than in 304 L manufactured by the same method. This difference in cellular coarsening for 316 and 304 was primarily attributed to molybdenum segregation at the cell boundaries [14]. For prolonged heat treatment times (2–400 h) at intermediate temperatures (600–800 °C), (not surprisingly) precipitation of carbides at high-angle grain boundaries (HAGB) was observed in several studies [11,14,15]. Yin et al. also observed that the formation and growth of the σ-phase at 800 °C occurred faster in AM 316 L than in wrought 316 L, which is most likely a consequence of Cr/Mo segregation and the presence of dislocation structures [11]. The development of σ-phase after annealing at 800 °C for 5 h was confirmed by Kurzynowski et al. [16]. High temperature annealing is generally observed to cause grain growth [10,17] and, eventually, recrystallization (or abnormal grain growth) and formation of equi-axed austenite grains at temperatures $\geq$1200 °C [18]. So far, only little research was dedicated to understanding the evolution of the amorphous silicates during heat treatment. Chen et al. suggested that increased silicate precipitation occurred during annealing at low temperatures (400–500 °C), while precipitate dissolution and coarsening were proposed during annealing at 800 °C [9]. An observed increase in hardness at this temperature was assumed to be related to more abundant precipitation [9]. Zhou et al. observed precipitation of additional silicon oxides at annealing temperatures of 1100 °C at grain boundaries, which resulted in reduced corrosion resistance [19]. Contrary to most other research, Yan et al. found crystalline nano-scale $MnSiO_3$ rhondite particles in the as-built condition; during heat treatment at 1200 °C these silicates transformed into a $MnCr_2O_4$ spinel phase [20].

The present contribution is dedicated to understanding the unconventional hierarchical as-built microstructure in 316 L austenitic stainless steel produced by L-PBF and, in particular, how this microstructure evolves in the temperature range 400–1100 °C. Specialized techniques such as particle extraction replicas and transmission Kikuchi diffraction (TKD) are applied to investigate the fine microstructural features in great detail. Specific attention is paid to the systematic investigation of the thermal evolution of the precipitates formed during LPBF of austenitic stainless steel.

2. Materials and methods

Specimens were manufactured by the L-PBF process on a Concept Laser M2 printer using gas atomized powder recycled as a mix of two powder batches. The powder particles in these two batches had a median diameter of 29 μm and the average chemical composition

Table 1
Chemical composition of powder as provided by the supplier.

	Fe	C	Cr	Mn	Mo	Ni	P	S	Si
Min [wt%]	Balance	–	16.5	–	2	10	–	–	–
Actual [wt%]	Balance	0.021	17.6	0.96	2.21	12.5	<0.03	0.006	0.52
Max [wt%]	Balance	0.03	18.5	2	2.5	13	0.05	0.03	1

is presented in Table 1. Oxygen and nitrogen contents in the powders were not provided by the supplier but were determined in the as-built parts by inert gas fusion analysis on a LECO TC500. The oxygen content was determined as ~0.04 wt%, while nitrogen content was measured to ~0.09 wt%.

The as-built specimens consisted of Ø10 × 30 mm cylinders; the build direction is parallel to the cylinder axis. An island scan strategy with parallel lines within the islands was employed. The islands were 5 × 5 mm^2 and parallel line scans in adjacent islands were rotated 90° with respect to each other. The islands were shifted 1 mm in both x and y direction for consecutive layers. The most important process parameters are collected in Table 2.

The specimens were heat treated in a Netzsch STA449 F^3 thermobalance, where heating and cooling rates are accurately controlled. A protective atmosphere of argon was applied during the treatments and all measurements and analyses were conducted in the bulk of the specimen (~1 mm from the surface), so the influence of surface reactions, as for example N_2 evaporation, can be excluded [21]. A heating rate of 20 K/min was applied until reaching 50 K below the setpoint temperature, from where the heating rate was reduced to 5 K/min to avoid temperature overshoot. The cooling rate was maximized to 50 K/min. Treatment temperatures and holding times are found in Table 3.

The 30-mm-high cylinder was divided into two parts. The two parts were subjected to different heat treatments. After heat treatment, sectioning was applied for transmission electron microscopy (TEM), scanning electron microscopy (SEM) and light optical microscopy (LOM) as illustrated in Fig. 1.

LOM was conducted on a Zeiss Axio Vert. A1 inverted light microscope. Specimens were etched prior to LOM. As-built specimens and specimens heat treated at temperatures ≤800 °C were etched by 20 min submersion in a solution of 1% HF and 5% HNO_3. Specimens, which were heat treated at higher temperatures, were etched in a diluted aqua regia solution with a 30 s swab to reveal relevant microstructural features and changes. Vickers micro-hardness measurements were conducted on polished specimens on a FutureTech FM-700 micro-hardness indenter using a load of 200 g and a 10 s dwell time. Ten repetitions were conducted for each sample. SEM was conducted on electropolished specimens on a Zeiss Supra FEGSEM equipped with a back-scatter electron (BSE) detector using a 60 μm aperture and an acceleration voltage of 20 kV. TEM was conducted on a Jeol 3000 F TEM using 300 kV acceleration voltage. Thin foil investigations were conducted on ground and twin-jet electropolished samples using an electrolyte consisting of perchloric acid ($HClO_4$) in ethanol at −40 °C. Investigation of inclusions and precipitates was conducted using extraction replicas, where a carbon film was deposited onto a slightly etched specimen, which was then electropolished in a solution of 5% HCl in ethanol to dissolve the matrix material and retain the particles in the replica. The carbon replica was mounted onto a copper grid for use in the TEM sample holder. Energy dispersive spectroscopy (EDS) was conducted in the TEM. TKD measurements were performed on an FEI Nova Nanolab 600 with a Bruker e-flash EBSD detector, and the Optimus detector head. The measurement was performed in a high vacuum at 30 keV beam energy, with an aperture of 30 μm and beam current of 1.7 nA. The map was acquired with a step size of 20 nm and a pattern resolution of 800 × 600 pixels with an exposure time of 88 m s per point. X-ray diffraction (XRD) was conducted on a Bruker D8 Discovery diffractometer using a locked-couple focusing principle and a scan range of 30–160 °2θ. A step size of 0.04 °2θ/step was applied along with a scan time of 7 s/step. Incomplete pole figures were determined by applying 0–70° ψ tilt and 0–360° φ rotation, both in steps of 5°, with a 1.5 s counting time for each combination of tilt and rotation angles.

Calculation of phase diagrams (CALPHAD) modelling was conducted using Thermo-Calc 2019 using the Fe6.2 database.

3. Results and interpretation

3.1. Characterization of the as-built condition

An X-ray diffractogram for a cross section along the cylinder axis, i.e. along the build direction is given in Fig. 2a. The as-built specimen is fully austenitic, and no indications for δ-ferrite were detected. In addition to the fcc peaks resulting from diffraction of Cr K_α radiation, a small peak originating from diffraction of K_β radiation by {200} austenite planes is observed at 71 °2θ. Fig. 2b shows the incomplete pole figures for the 111, 200 and 220 reflections of austenite, measured on a *xy* cross section perpendicular to the cylinder axis, i.e. within the build plane. All pole figures show a tetrad symmetry reflecting the 90° rotation between line scans in adjacent islands. This is analogous to previous research, where a 67° rotation between consecutive layers was reflected in the crystallographic texture [21]. In Fig. 2b, the {220} planes are preferably oriented perpendicular to the build direction, while the {111} and {200} planes are inclined with respect to the build direction.

Light optical micrographs of the as-built condition are presented in Fig. 3. In the cross section, the melt pools have a spherical cap morphology, approaching the geometry of semi-circles (Fig. 3a). Austenite grains extend over multiple melt pools and are strongly elongated along the build direction. At higher magnification (Fig. 3b), the cellular structure inside the austenite grains is observed. Analogous to the continuation of austenite grains over melt pool "boundaries", cells with a specific orientation inside an austenite grain can continue across such "boundaries".[2]

BSE SEM micrographs are presented in Fig. 4. At low magnification, Fig. 4a and -b, an overview of the microstructure is obtained, showing an intricate pattern of grey tones caused by channelling contrast. Also, two rather large pores are identified (see white arrows in Fig. 4a), which are defects from the printing process. The cellular structure is clearly observed at higher magnification (Fig. 4c). The cell walls appear bright, indicating that elements with a higher atomic number than average (in this case Mo) for the alloy are

[2] Strictly speaking, the continuation of an austenite grain and substructure across this morphological feature would not be reconcilable with the criteria for a boundary, wherefore it is given in quotation marks here.

Table 2
Main process parameters for the L-PBF fabrication.

	Power [W]	Speed [mm/s]	Hatch spacing [μm]	Layer thickness [μm]
Border contour	150	350		
Bulk	180	350	120	30

Table 3
Heat treatment parameters.

Temperature [°C]	400	500	600	700	800	900	1000	1100	1100
Time [min]	60	60	60	60	60	60	60	60	120

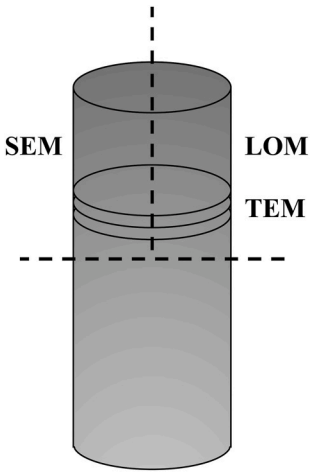

Fig. 1. Sectioning of L-PBF specimens, prior to heat treatment and for characterization.

segregated there. In addition, the high dislocation density at the cell walls is held responsible for the brighter appearance, because electrons cannot channel as deep as in the cell interiors. The small black and white dots in Fig. 4c are interpreted as inclusions. The observations are consistent with earlier observations in the literature. The cells are columnar, as follows from Fig. 4c, where some cells appear to be almost equi-axed in shape (within white circle), while others appear to consist of parallel lines (red circle). The appearance of the cells in cross section depends on their orientation with respect to the cross-sectional plane. When the cells are cut perpendicular to their column axis, they will appear equi-axed; cells cut parallel to the column axis appear as parallel lines.

The cellular structure is shown in greater detail in the TEM micrographs in Fig. 5. The cell walls consist of a dense network of dislocations. Dislocations are also present in the interior of the cells, albeit at appreciably lower density (Fig. 5c). The electron diffraction pattern for the area shown in Fig. 5a is presented in Fig. 5b. The pattern is a typical image along the <110> zone axis of fcc crystals, implying that the cells axis is parallel to <110>. The pattern consists of several overlapping diffraction patterns with a small rotation angle (misorientations) between them. Dark field images from three diffraction spots are presented in Fig. 5d–f. The different diffraction spots belong to different parts of the cellular microstructure, i.e., different groups of cells. This means that not all cell walls incur a misorientation, but rather that groups (domains) of cells have a specific misorientation with respect to adjacent domains within the same, large, austenite grain. The misorientation between groups of cells is corroborated by the BSE image in Fig. 5c. Here, groups of equi-axed cells (domains) show different channelling contrast, indicating a (slight) difference in orientation. Besides the domain misorientation observed in the diffraction pattern in Fig. 5b, smaller diffraction spots around the main fcc spots primarily originate from diffraction in the cell walls (Fig. 5d).

The misorientation between domains of cells was further investigated with transmission Kikuchi diffraction (TKD). In Fig. 6 the bright field image on the left shows differently oriented cells, which belong to two different austenite grains; the grain boundary is marked by the white arrows. The pattern quality (PQ) map hardly reflects the cell structure as observed in bright field image but indicates “boundaries” between groups of cells. This is further supported by the orientation maps (both Euler and colouring according to the standard stereographic projection triangle, also referred to as IPF colouring), where all misorientation is accumulated in domain walls rather than in individual cell walls. In the Z direction (i.e. the build direction) no misorientation between domains is observed, implying that misorientations within this austenite grain are limited to rotations about the cylinder axis of the specimen. The kernel average misorientation (KAM) in the upper right corner of Fig. 6, is maximally 4.3° and limited to a very small region that separates neighbouring domains. At other locations, maximum misorientations between domains of 2–3° are found.

The as-built microstructure also contains nano-scale spherical particles, which often correlate with the location of the cell walls

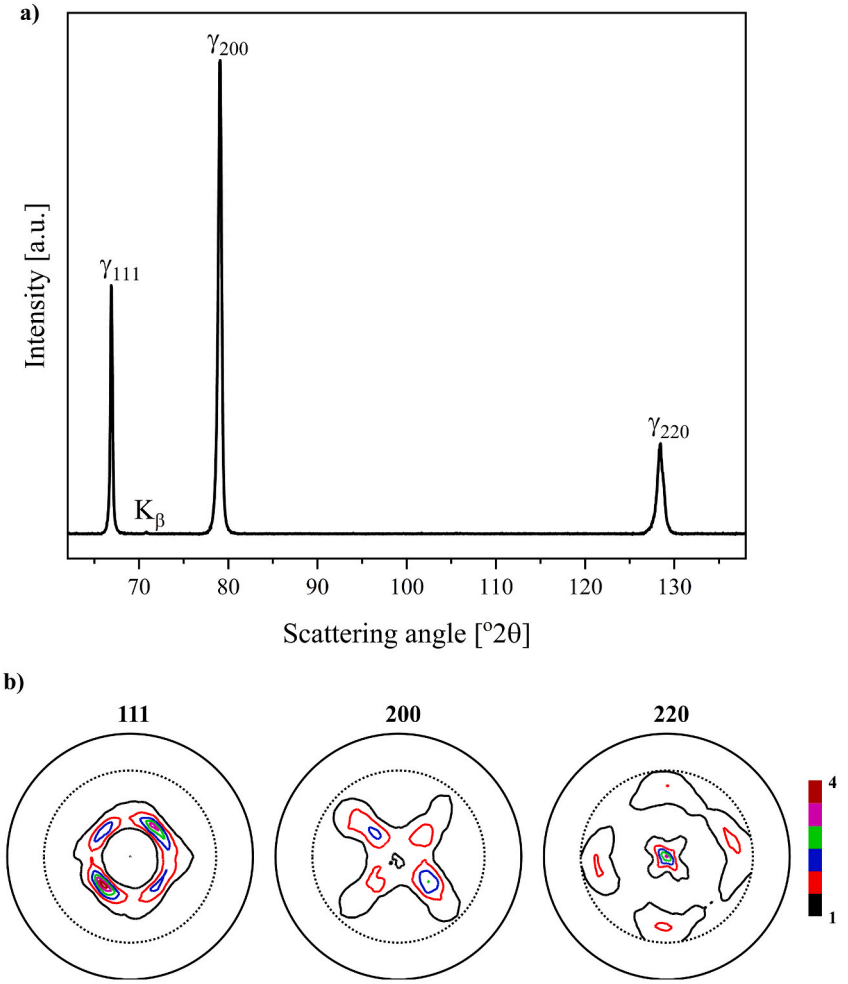

Fig. 2. XRD measurements on the as-built condition. a) X-ray diffractogram measured across build planes, b) XRD incomplete pole figures measured on the build plane.

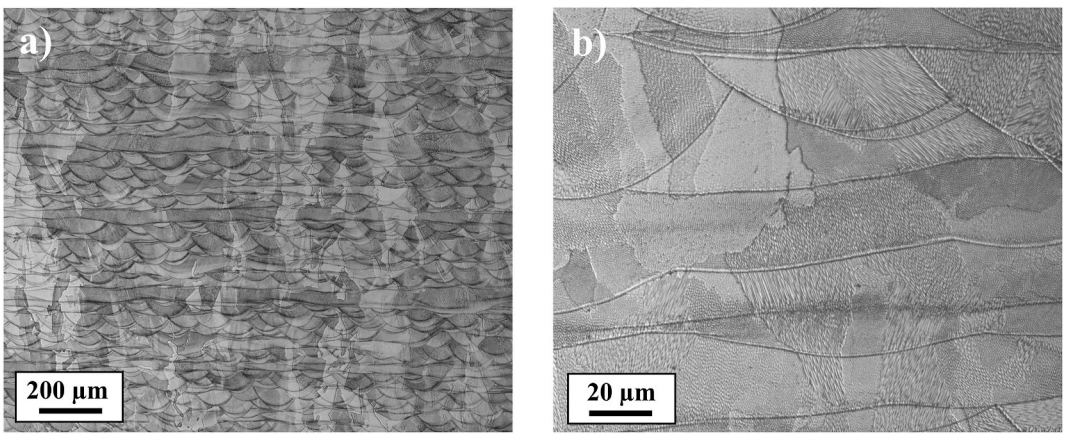

Fig. 3. LOM micrographs of the as-built microstructure. Build direction from bottom to top.

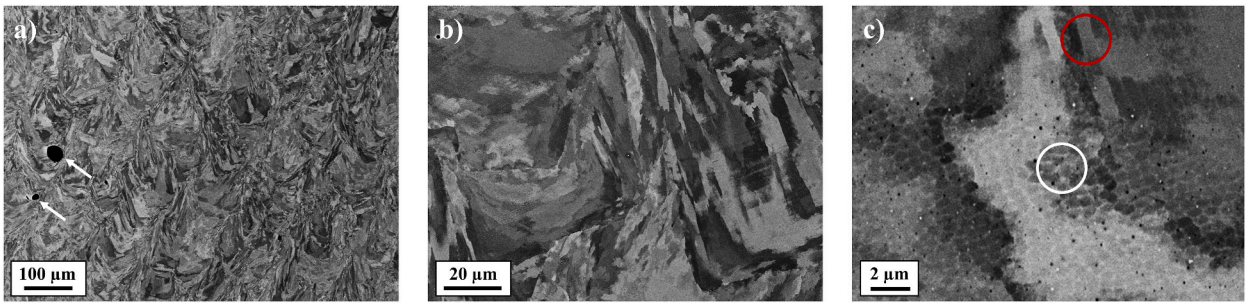

Fig. 4. SEM BSE micrographs of the as-built condition. The white circle marks equi-axed oriented cells. The red circle marks transversely oriented cells. Build direction from bottom to top.

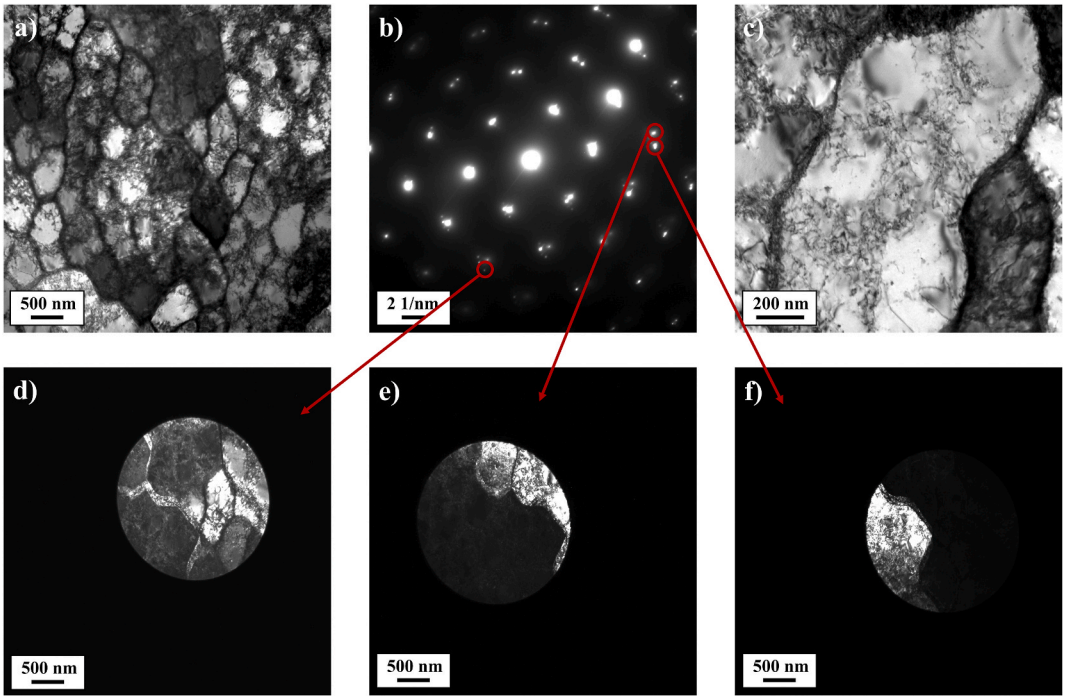

Fig. 5. TEM micrographs of the as-built condition. a) Bright-field overview, b) diffraction pattern of microstructure in a), c) bright-field detail, *d*-f) dark-field micrographs of a).

(Fig. 7a and -b). These particles are amorphous. The dark field image in Fig. 7d is taken from the location of the amorphous ring in the diffraction pattern away from the fcc spots (Fig. 7c). Dark field imaging reveals the presence of an additional particle (Fig. 7d, top), which is obscured by dense dislocation tangles in the bright field image in Fig. 7b.

It was not possible to quantitatively determine the composition of the particles using thin foil specimens due contributions of the austenite matrix to the EDS signal. Therefore, the particles were removed from the matrix using the carbon extraction replica method. The bright field TEM micrographs of the particles extracted using this replica method are shown in Fig. 8. At low magnifications (Fig. 8a), a network is observed, reminiscent of the cell structure in the thin foil specimens (Fig. 5a). This network is observed as dark lines on the replica. Amorphous spherical particles are located along these lines decorating cell walls and the cell interior. The composition of spherical particles and cell wall lines is presented on the Gibbs triangles in Fig. 8c. These composition maps include the main metallic elements (Si, Mn, Cr, Fe, Mo). In Fig. 8c Mn and Si have their own axis and Fe, Cr and Mo share an axis; in Fig. 8d Fe, Mo and Cr each have their own axis. Oxygen is omitted from the maps because the quantification of light elements with EDS is not as accurate as heavier elements. Nevertheless, both the spherical particles and the cell wall lines contain a significant amount of oxygen in addition to the metallic alloying elements. The metallic compositions are normalized to a total of 100 at.%, so this figure shows the ratio between the metallic elements rather than the actual composition. For most measurements on the lines, Fe, Cr and Mo constitute 80–90 at.% of the metallic composition (excluding O). The spherical particles consist mainly of Si with small contents of Mn and Cr (the latter is contained in the Cr + Fe + Mo axis in Fig. 8c). The content of these elements varies from particle to particle. However, the

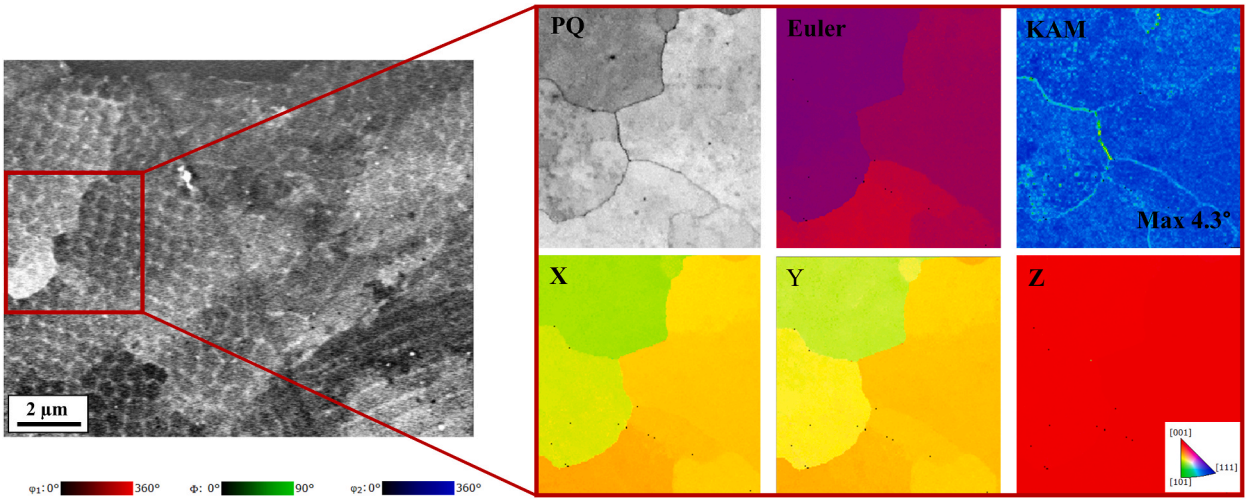

Fig. 6. TKD results on the as-built condition. Top, left: Quality of Kikuchi patterns. Top, middle: orientation according to Euler angles. Top, right: Kernel average misorientation map (3 × 3). Bottom: Orientation of the grain with respect to the X, Y, and Z axis (Z = Build direction).

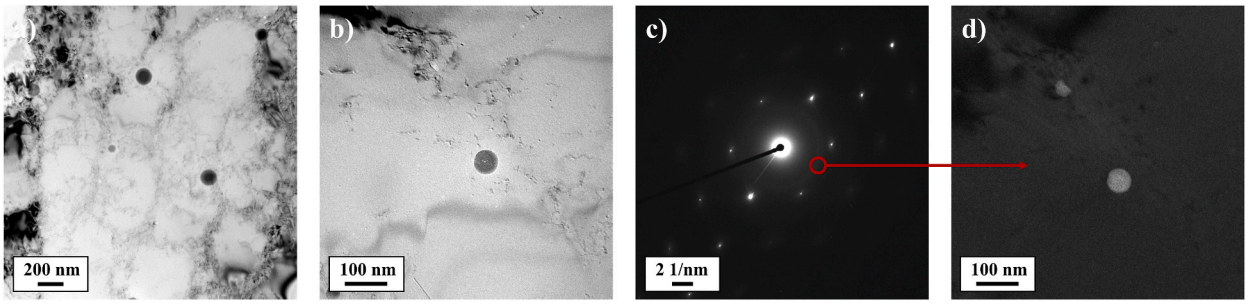

Fig. 7. TEM micrographs of the as-built condition. a) Bright-field overview of particles, b) bright-field detail, c) diffraction pattern of b), d) dark-field micrograph of b).

spherical particles are consistently Si-rich (>50 at.% Si). Accordingly, these spherical particles are identified as amorphous Mn,Cr-silicates. The cell wall lines have a different composition. While still high in oxygen, these features contain barely any Mn and have much lower contents of Si than the spheres. Instead, they are particularly rich in Cr along with Fe (<40 at.%) and Mo (Fig. 8d).

3.2. Characterization of the heat-treated condition

The evolution of the hardness in the bulk of the heat treated and as-built samples is presented in Fig. 9. The measured hardness of 241 ± 6 $HV_{0.2}$ for the as-built condition is higher than for conventionally manufactured AISI 316 L [22], but consistent with other L-PBF produced specimens of this steel [23–25]. Interestingly, there is a slight increase in hardness after 1 h heat treatment at 400 °C to 256 ± 7 $HV_{0.2}$. With increasing temperature, the hardness decreases gradually to the lowest measured hardness value of 193 ± 8 $HV_{0.2}$ at 1100 °C.

3.3. Morphology

An overview of LOM micrographs for different heat treatment temperatures is provided in Fig. 10. At low temperatures (≤800 °C, see Fig. 10a–e), very few changes in the microstructure are observed. At 800 °C, the cell structure appears fainter, but is still visible. The shape and size of the austenite grains appear unchanged. At 900 °C (see Fig. 10f), the cellular structure has largely dissolved, but melt pool "boundaries" remain visible, albeit faintly, indicating that the cellular structure is less stable than the melt pool boundaries. For 1000 °C and above (see Fig. 10g–i), the melt pool structure has disappeared and only the elongated austenite grains remain.

BSE micrographs in Fig. 11 confirm that the cellular structure disappears with increasing heat treatment temperature. Up to 700 °C (see Fig. 11a–d), the microstructure appears unchanged as compared to the as-built condition (cf. Fig. 5). Bright cell walls are visible along with small black particles. At 800 °C (Fig. 11e), the bright walls of the cellular structure are barely visible, while the fine structure of the austenite matrix is retained. Even though the cellular structure is no longer present in the samples heat treated at 900 and 1000 °C (see Fig. 11f and -g), the fine austenite misorientation structure, further referred to as domain structure, is retained. This

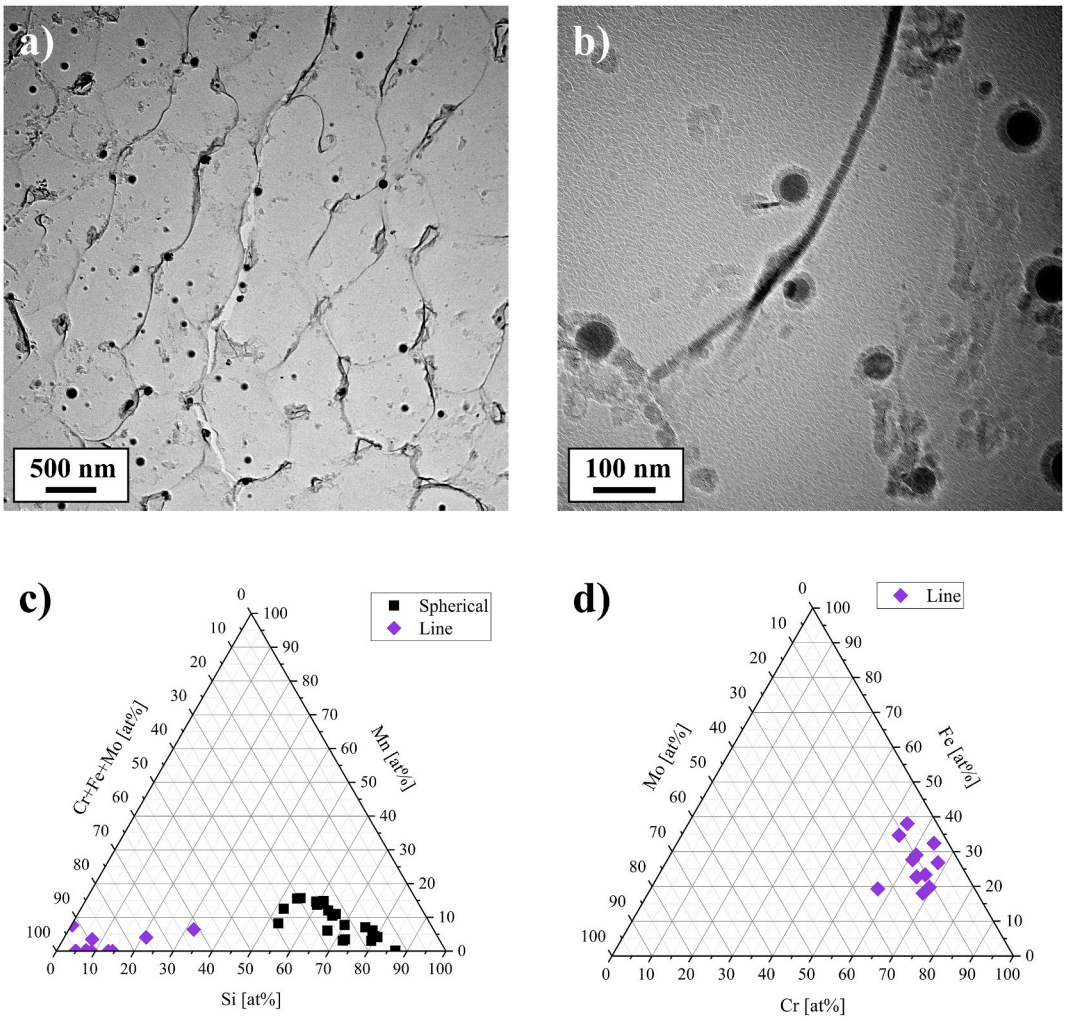

Fig. 8. a) and b) TEM micrographs of replicas extracted from the as-built condition. c) and d) Particle composition maps as obtained using EDS on this replica. Black squares: Si-rich oxides. Purple diamonds: Dark lines.

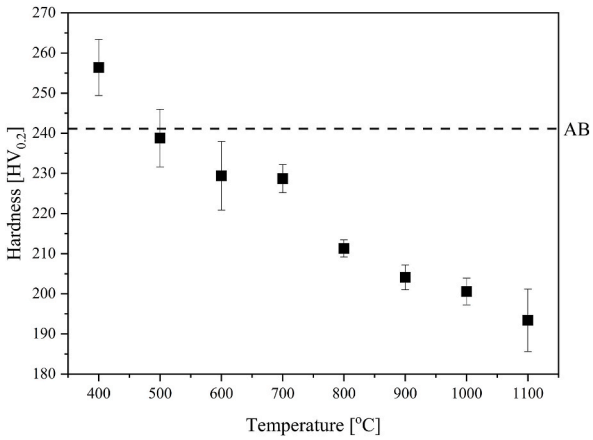

Fig. 9. Hardness measurements for different heat treatment temperatures for L-PBF 316 L. 1 h duration. All results are averaged over at least 10 data points.

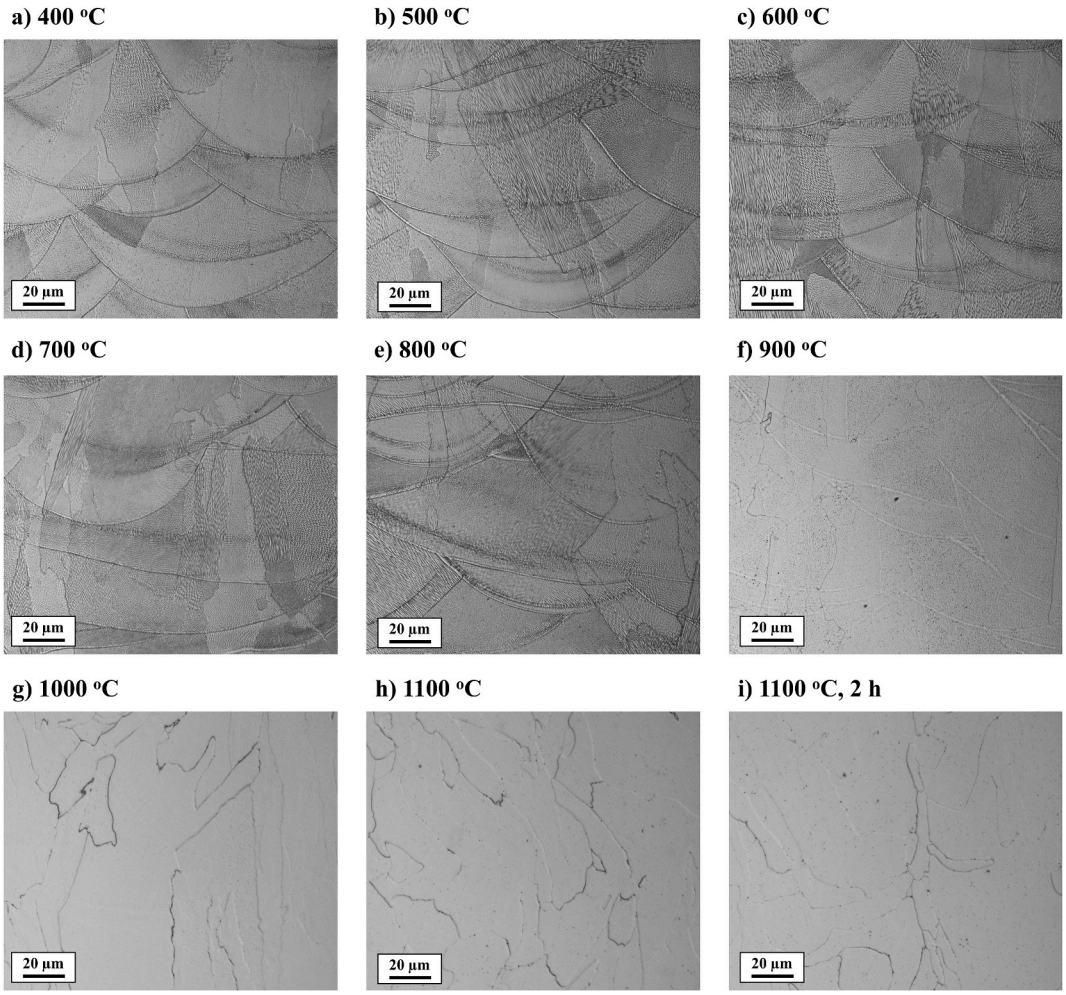

Fig. 10. LOM micrographs of specimens heat treated at different temperatures for a duration of 1 h, otherwise specified. Build direction from bottom to top.

means that the domain structure, characterized by small orientation differences between the domains, remains, even after the bright cell walls have dissolved. At 1100 °C the domains grow (compare Fig. 11h and -i for 1 h and 2 h, respectively), while a very fine internal structure within the large austenite grains is retained. Evidently, heat treatment at 1100 °C is insufficient to change the morphology of the as-built elongated austenite grains, because no equi-axed grains were observed. Furthermore, for temperatures ≥1000 °C the black particles in the steel matrix grow in size.

Applying TEM (Fig. 12), it is observed how the cellular dislocation-segregation structure evolves with the treatment temperature. The dislocation density along the cell walls is reduced from 500 °C and above and the walls become diffuse around 800 °C, compare Fig. 12a–f. At high temperatures, the domain boundaries remain (Fig. 12g–i). Domains show slightly different diffraction contrast, indicating a difference in orientation. At 1100 °C (Fig. 12h and -i), the domains appear to have grown slightly as compared to the as-built condition and lower treatment temperatures. Furthermore, large oval particles are observed at this temperature. In Fig. 12h, the particles appear to be located primarily along the domain boundaries, suggesting that they impede the movement of the domain boundaries. At several locations the (larger) particles along domain boundaries have fallen out of the thin foil specimens, leaving bright holes.

Additional TEM micrographs after heat treatment at 900–1100 °C are given in Fig. 13. Here, patterns of particles reminiscent of the cell structure are visible, although the cells dissolved at around 800 °C (Fig. 12). Apparently, particles have precipitated preferentially along former cell walls and domain boundaries (marked by black arrows in Fig. 9a–c).

3.4. Evolution of inclusions and precipitates

The evolution of the amorphous silicon oxides as a function of heat treatment temperature is further investigated using carbon extraction replicas. Bright field TEM micrographs of extraction replicas for treatment temperatures ranging from 600 to 1100 °C are

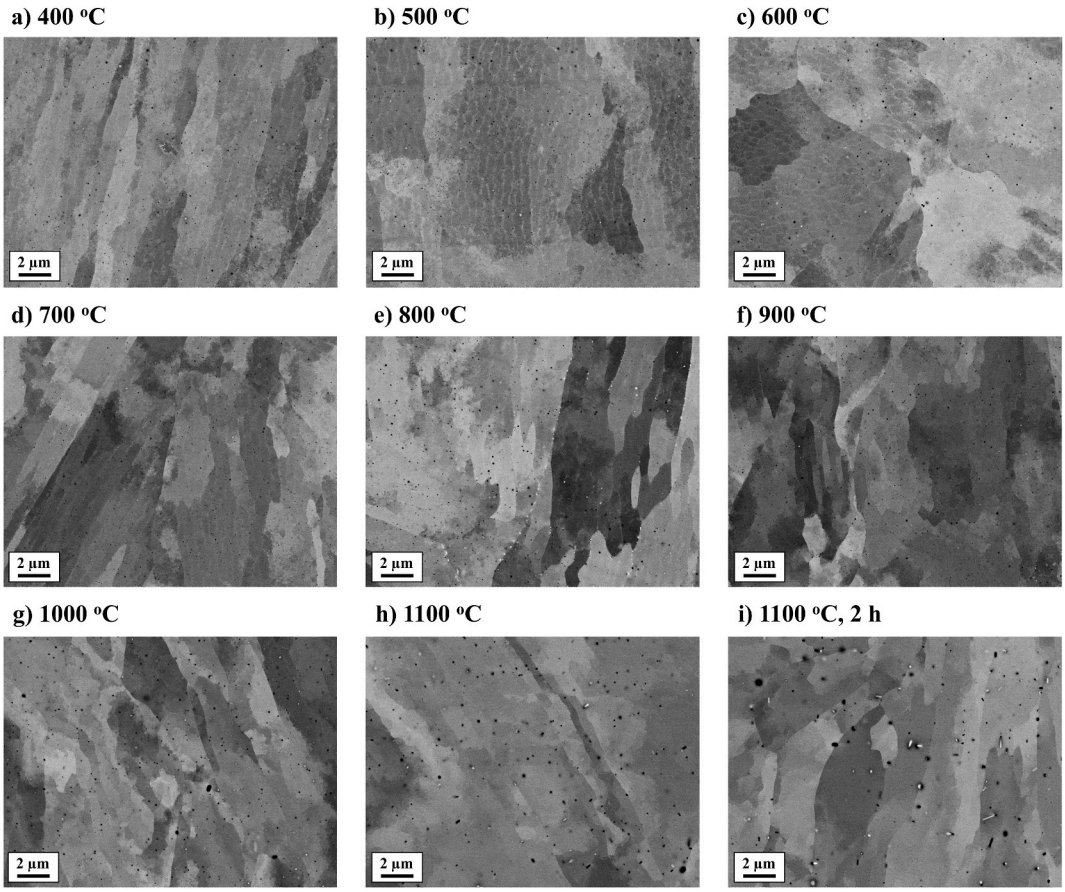

Fig. 11. SEM micrographs of the heat treated conditions. a)-h) 1 h duration. i) 1110 C, 2 h duration. Build direction from bottom to top.

presented in Fig. 14. The specimen treated at 600 °C (Fig. 14a) exhibits very similar particle sizes and morphology as the as-built condition (Fig. 8). At 700 °C (Fig. 14b), the particles start to change significantly in size, shape and crystallinity. Very dark particles of irregular shape have developed adjacent to the spherical particles (see arrows). These spherical particles are of similar size as those in as-built and 600 °C annealing conditions. At some locations, these dark particles are present without a lighter spherical particle as an immediate neighbour, while at other locations only the original spherical particles are present. These observations suggest that the development of the dark irregular particles occurs gradually and that their formation (or transformation) is not complete within 1 h at 700 °C. At 800 °C (Fig. 14c), the particles show a similar effect, with light and dark particles separating even further and mainly the dark particles increase in size. Furthermore, some very small, light and spherical particles are present. At 900 °C (Fig. 14d), the pairs of light and dark particles have disappeared. Instead, dark oval or oblong particles are present in the material. These become very clear at 1000 °C (Fig. 14e). At 1100 °C (Fig. 14f), the elongated, oblong particles have grown larger and measure approximately 300 nm. Also, much smaller, round particles are present at this temperature. The large oblong particles are crystalline as seen in the inserted diffraction pattern in Fig. 14f. This crystallinity of the particles is observed from 900 °C and above.

The dual light/dark particles observed at 700 °C were further investigated in Fig. 15a with convergent beam electron diffraction (CBED). As with the spherical light particles in the as-built specimen, the light part of the particle is amorphous (Fig. 15c), while the dark particle is crystalline (Fig. 15b).

Composition maps of analyzed particles are presented in Fig. 16. At 600 °C (Fig. 16a), the particles consist mainly of silicon and oxygen (as for the as-built condition, Fig. 8c). At 700 °C (Fig. 16b), two families of particles can be discerned. The light particles have a composition similar to the one found at 600 °C (and the as-built condition), albeit with a larger variation in manganese content. The dark particles consist almost entirely of Cr, Fe and Mo, with a very low or no oxygen signal (not shown). Using selected area electron diffraction (SAED) these dark precipitates are identified as the tetragonal σ-phase. This trend is also observed for the specimen heat treated at 800 °C (Fig. 16c), where the round silicon oxides contain a variation in manganese content. The dark particles do not contain oxygen and consist mainly of Cr, Fe and Mo. The round particles with a high manganese content tend to be very small and are located away from the dark particles (see arrows in Fig. 14c), while the particles with a composition similar to those in the as-built structure (Fig. 8c) are located adjacent to the dark particles.

The compositions of the dark particles at 700 °C and 800 °C are compared in Fig. 17 on a Cr, Fe, Mo Gibbs triangle. As mentioned, the composition of these elements is normalized, so the figure only shows the ratio between the elements, not the actual composition.

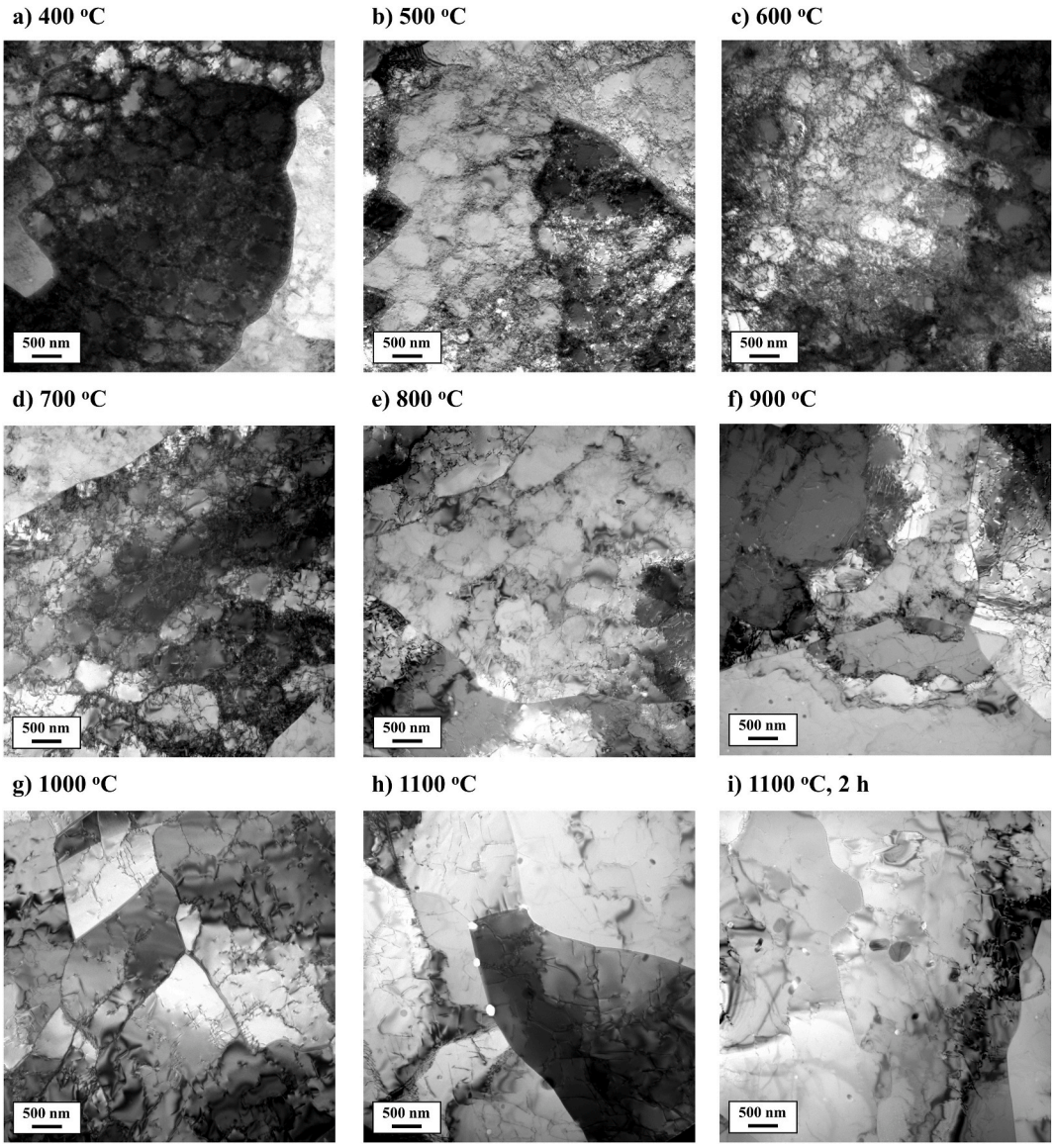

Fig. 12. TEM micrographs of the specimens heat treated at different temperatures 400–1100 C. a-h) 1 h duration, i) 1100 C for2 h duration.

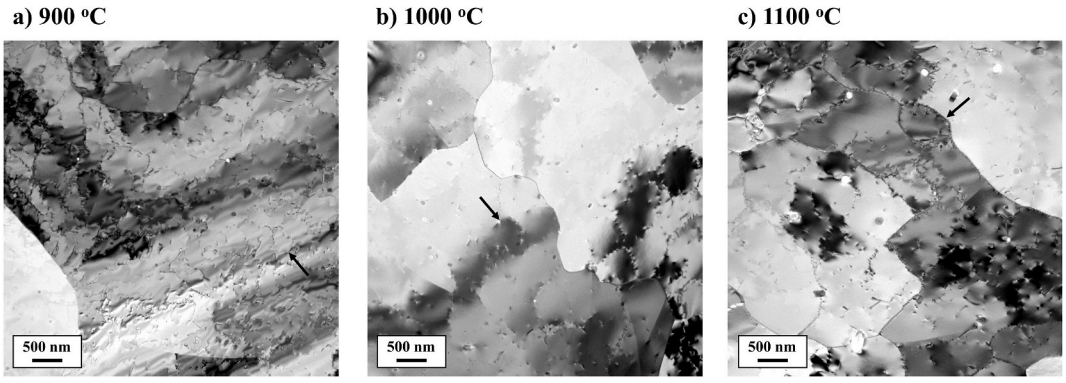

Fig. 13. TEM micrographs of specimens heat treated for 1 h at a) 900 °C, b) 1000 °C and c) 1100 °C. Black arrows mark examples of precipitates formed at former cell walls.

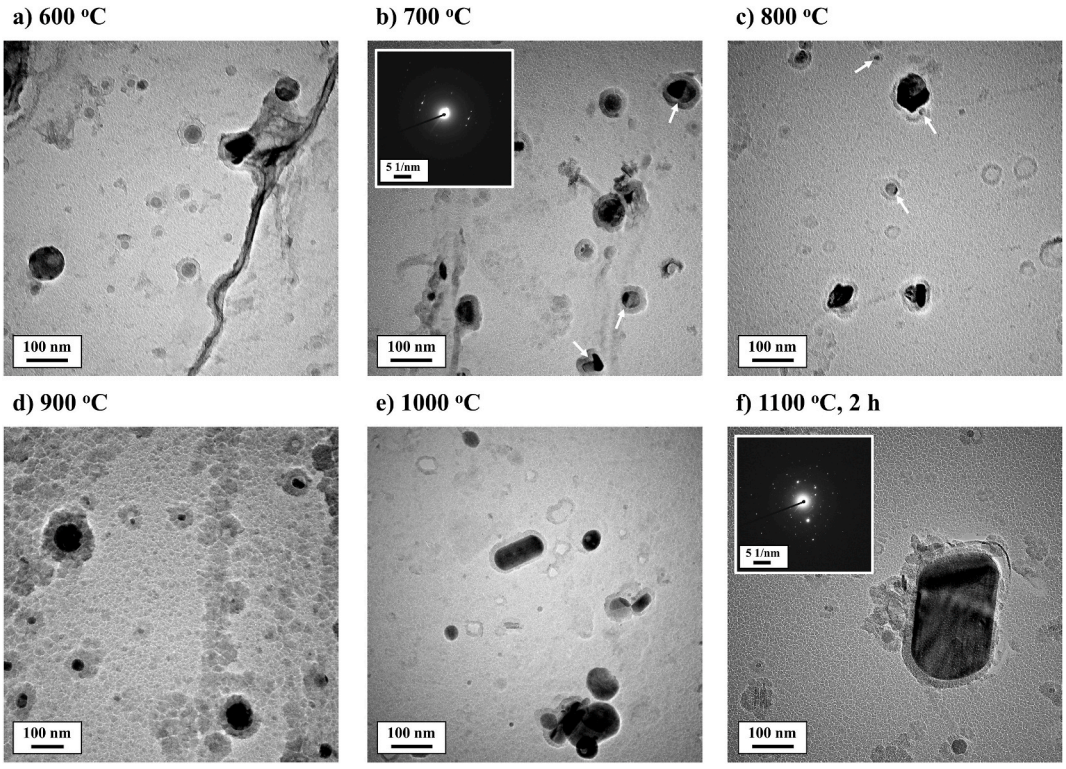

Fig. 14. TEM micrographs of the heat treated conditions. Particles extracted using the carbon replica method. The crackled appearance is inherent to the replica, while the (crackled) halos around particles are caused by bending of the replica under the weight of the particles.

Changing the heat treatment temperature from 700 °C to 800 °C leads to an enrichment of Mo and Cr in the σ-phase precipitates. At 900 °C, σ-phase precipitates have disappeared. Instead, the round particles observed in Fig. 16d consist of silicon and manganese in varying ratios. As compared to the as-built (Fig. 8c and d) and 600 °C (Fig. 16a) condition, the particles at 900 °C are rich in manganese and maintain a high oxygen content. At 1000 °C (Fig. 16e), these silicon-manganese oxides are still present, but their composition appears to vary less abundantly. These particles have low or no Cr, Fe and/or Mo. A single particle of the Cr and Mn-rich oxide type is also observed at this temperature (green triangle). This particle also has a high titanium content (~12 at%), which is not included in the composition maps. After a 2 h treatment at 1100 °C (Fig. 16f), two distinct particle compositions are distinguished: large, oblong silicon-manganese oxides and small, round manganese chromium oxides. A particle with a composition similar to the as-built condition (silicate with a lower manganese content) persists.

4. Discussion

4.1. As-built condition

The microstructure of L-PBF produced austenitic stainless steel is very different from conventionally produced material and is hierarchical in nature with microstructural features at different length scales. The hierarchical microstructure is illustrated in Fig. 18.

The largest features are the melt pools with spherical cap morphology, where the width of the melt pools is comparable to the width of the laser beam, i.e. around 100 μm. The height of the melt pool is related to the thickness of the added powder layer and the applied laser power. The process parameters need to be optimized to ensure full melting of the powder layer as well as part of the, underlying, previously solidified material. In this manner, the risk for so-called lack-of-fusion porosity can be limited [26]. Lack of fusion pores are large and irregular/triangular in shape and highly detrimental for the mechanical properties, because the sharp corners act as stress concentrators [26,27]. The porosity observed in Fig. 4 is spherical and originates from gas entrapment and/or melt pool instabilities. The spherical shape is much less detrimental to the mechanical properties than irregularly shaped lack-of-fusion pores [2]. The elongated austenite grains constitute the next level in the hierarchical microstructure, even though they are of a similar (or larger) scale as the melt pools. In most cases, the elongated austenite grains grow across multiple melt pools. Accordingly, their orientation continues through the layer-wise building, indicating homo-epitaxial nucleation during solidification. At this stage, it is important to add another level to the hierarchy, which is usually not reported in the available literature on the microstructure of additively manufactured materials. The cellular structure formed inside the elongated austenite grains has long been a source of discussion. The cells are often referred to as sub-grains [14,15,28,29], which appears unclear because sub-grains entail a misorientation structure, as

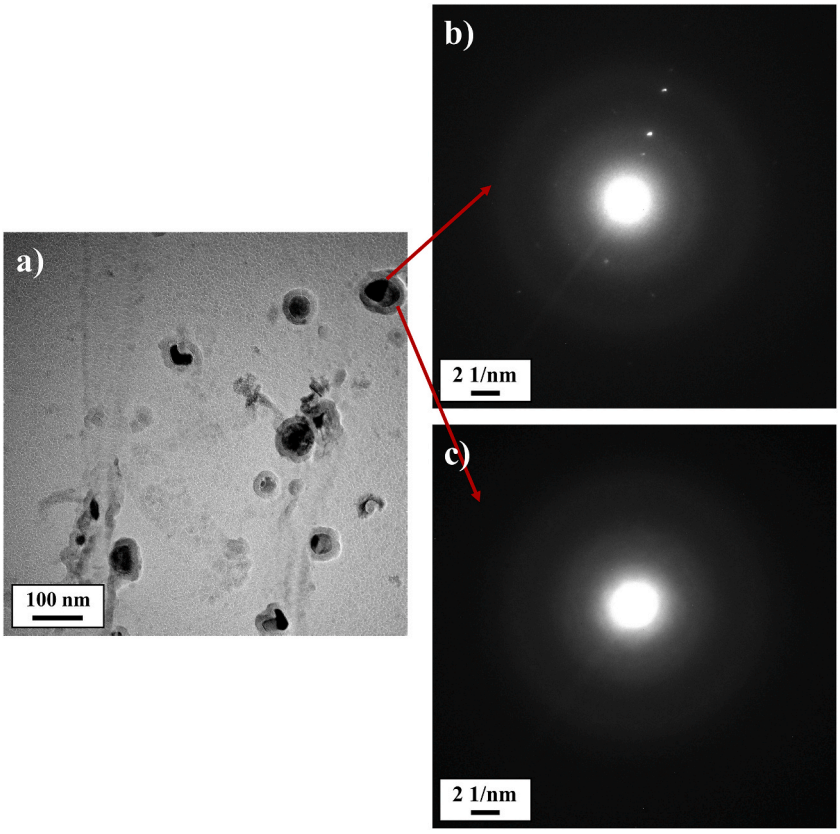

Fig. 15. Carbon replica of specimen treated at 700 °C (same as in Fig. 14b). a) bright field image, b) and c) convergent beam diffraction of dark and light region of the particle.

known from recovery in deformed materials [30]. In some literature sources it is speculated that each cells is misoriented with respect to their neighbouring cells [11,31,32]. Our investigations show that this is incorrect, but that cells are grouped in domains. Within a domain, all cells have the same orientation and low-angle grain boundaries occur between the domains (Figs. 5 and 6). This is consistent with observations and discussions by Voisin et al. [33]. The next level of hierarchical microstructure is the cellular structure itself, which is rather well documented in the literature. The cell walls have some degree of elemental segregation of primarily Cr and Mo and a high dislocation density is present along the walls. The cells are columnar in nature with a size of the short axis in the range of 400–700 nm and the long axis has a length of several microns up to the full length of the primary austenite grain. It is important to note that regardless of their appearance as either equi-axed cells, ellipsoid cells or parallel lines (depending on the cutting angle with regards to the cell orientation), they are the same cells and not two different types of cells or dendrites, as has been reported [9,18,28,34]. As the misorientation is constrained to domain boundaries, the cell walls do not originate from bridging the misorientation between neighbouring cells. Segregation of alloying elements in cell walls is often reported in the literature [3,11,14,35], but so far no research has been conducted using extraction replicas. Interestingly, the cell walls of the as-built structure included in the replicas contain higher contents of ferrite formers Cr, Mo and Si (relative to the overall composition and the cell interior) as well as oxygen. The cell wall lines are therefore interpreted as Fe,Mo-containing Cr-oxides. To explain this observation the following hypothesis, which has not been proposed earlier, is put forward. Initially, the solidification of AISI 316 L should result in a mixture of ferrite and austenite, i.e. a dual-phase structure. Directional solidification under the influence of a steep temperature gradient, because the solidified material of the previous layers functions as a heat sink, first leads to the formation of austenite cells, because austenite nucleates epitaxially on the previously solidified alloy. Accordingly, the liquid that surrounds the austenite columns is enriched in ferrite-forming elements and species with low solubility in austenite, for example, O. The liquid phase enriched in ferrite formers could solidify as ferrite and transform into austenite on continued cooling. Essentially, this transformation from ferrite to austenite could be reconstructive (e.g. massive) or displacive (e.g. martensitic). It is suggested that the volume change accompanying the ferrite-austenite transformation during cooling is responsible for the dislocation networks recognized as cell walls. Whether the inter-dendritic liquid enriched in ferrite stabilizers solidifies as ferrite will depend on the specific local composition and whether the ferrite can be retained at room temperature depends on the cooling rate [36]. Laser engineered net shaping process (LENS) is a MAM process, which is known to have a lower cooling rate than L-PBF. 316 L produced by the LENS technology results in a cellular structure with significant elemental segregation and a band of ferrite along the cell walls [37].

Several studies have investigated whether the strengthening effect of the cellular structure obeys a Hall-Petch relationship [3,32,

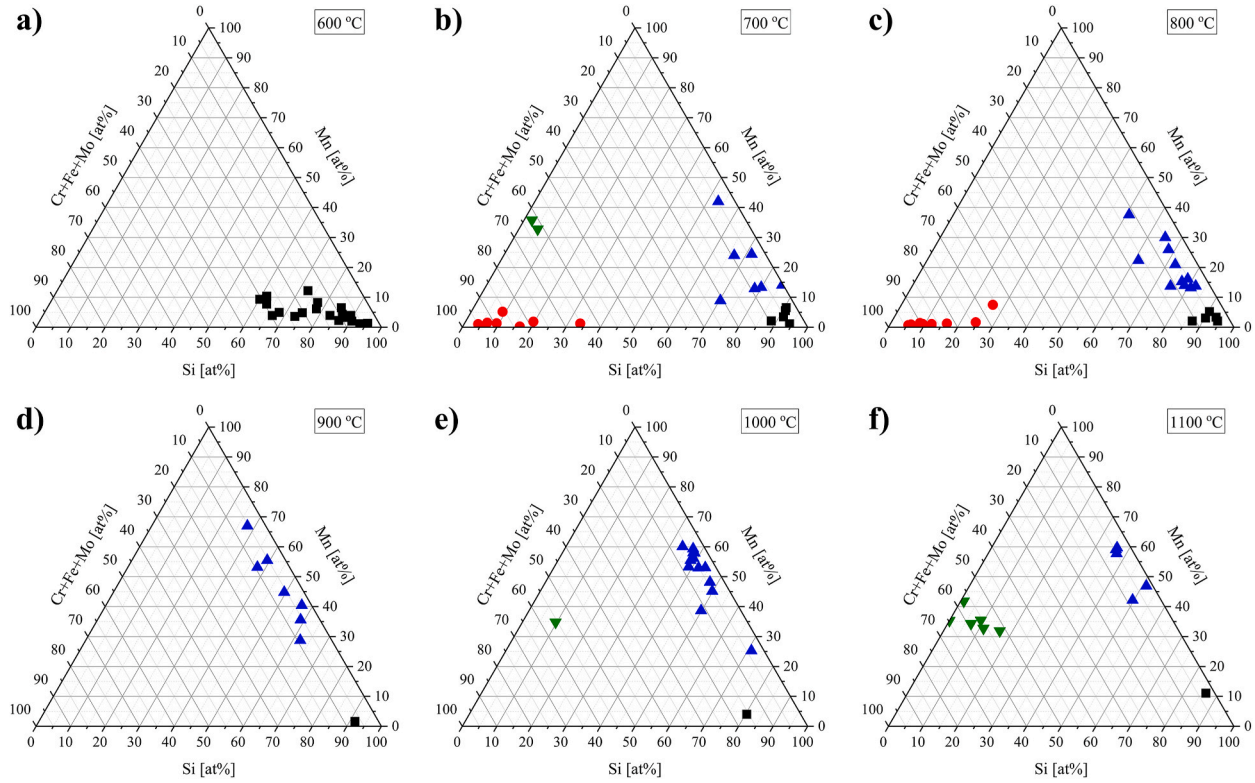

Fig. 16. Particle composition maps from EDS measurements of extraction replicas of heat treated specimens. Black squares: Si-rich oxides. Red circles: σ-phase. Blue triangles: Mn containing oxides. Green inverted triangles: Cr–Mn-rich oxides.

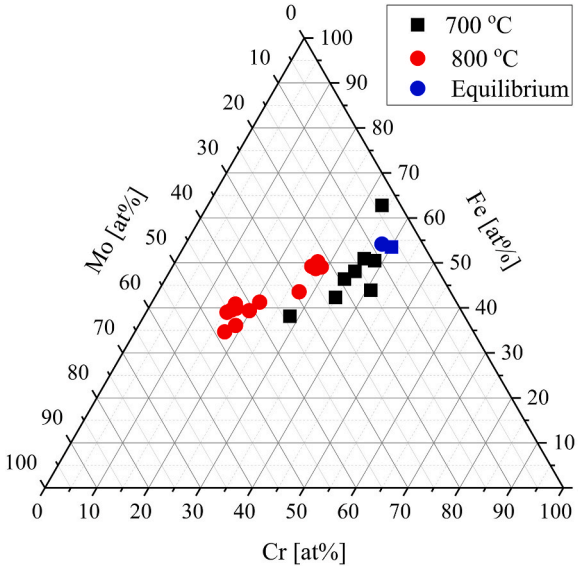

Fig. 17. Composition map from EDS measurements on dark particles in extraction replicas of specimens heat treated at 700 °C and 800 °C. Black squares: 700 °C. Red circles: 800 °C. Blue square and circle: Equilibrium composition for σ-phase at 700 °C and 800 °C respectively.

38,39]. Wang et al. found that strengthening using a Hall-Petch type relationship for the cell size accounted for a significant portion of the increased yield strength, but that also other strengthening effects contribute [3]. Krakhmalev found good agreement with the calculated Hall-Petch relationship and related discrepancies between measured and calculated strengths to local variations in cell size [39]. Bahl et al. argued that implementing the cell size in a Hall-Petch calculation may be problematic as the parameters are usually

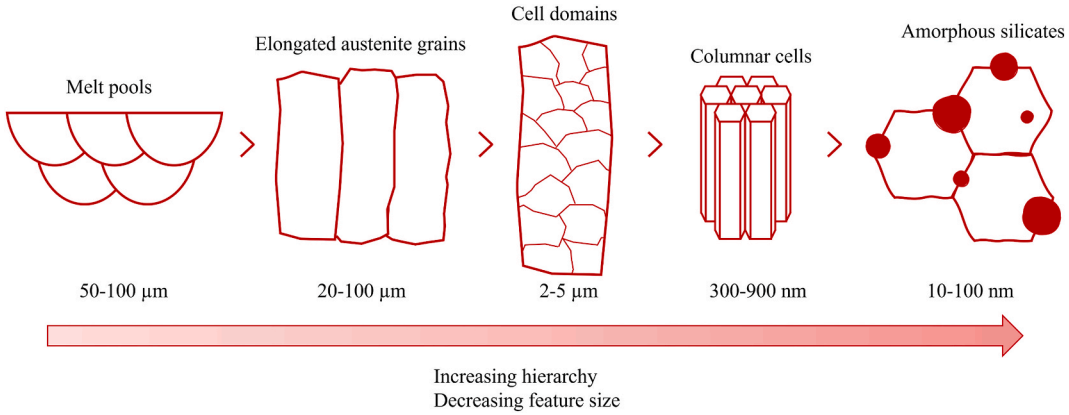

Fig. 18. Sketch of the unconventional hierarchical microstructure features found in as-built L-PBF austenitic stainless steel.

only applicable for high-angle grain boundaries. Instead, only a small strength contribution was associated with high-angle grain boundaries, while the majority of the strength was attributed to increased dislocation density [40]. The cell walls may not act as high angle grain boundaries, but the high dislocation density in the cell walls is likely to hinder dislocation movement, just like self-organized dislocation cell walls in deformed materials would do.

At a smaller length scale than the cellular structure, the spherical amorphous inclusions of Cr/Mn containing silicates range in size from 10 to 100 nm. It is well-known that the presence of fine particles can contribute to the strength of a material, as for oxide dispersion strengthened (ODS) steel. Nevertheless, the distribution density of the silicates in as-built 316 L material is considered too low to contribute significantly to the strength of the material [3,41]. Some investigations have attributed the higher strength of L-PBF 316 L over conventionally manufactured material to the presence of these inclusions [8,42]. It is however much more likely that a combined effect of dislocation networks, grain (or domain) size, crystallographic texture, elemental segregation and interstitially dissolved nitrogen content [3,43,44] is responsible for the mechanical performance of the material.

4.2. *Evolution of the cell structure*

The thermal stability of the unconventional microstructural features obtained by L-PBF of austenitic stainless steel is summarized in Fig. 19.

Under thermal exposure, the cell structure dissolves gradually. At the lowest investigated treatment temperature (400 °C), it was not possible to detect any changes in the microstructure using the applied characterization techniques. Nonetheless, an increase in hardness was observed. A similar hardness and associated yield strength increase was previously observed by Chen et al. who attributed it to the formation of inclusions during low temperature heat treatment [9]. However, no discernible difference in particle density was observed in this study and precipitation is rather sluggish at this temperature as it involves long range diffusion of substitutional elements. The possibility of static strain ageing needs to be considered here due to the high dislocation density along the cellular walls in combination with the interstitially dissolved nitrogen in the material. During static strain ageing, interstitial elements

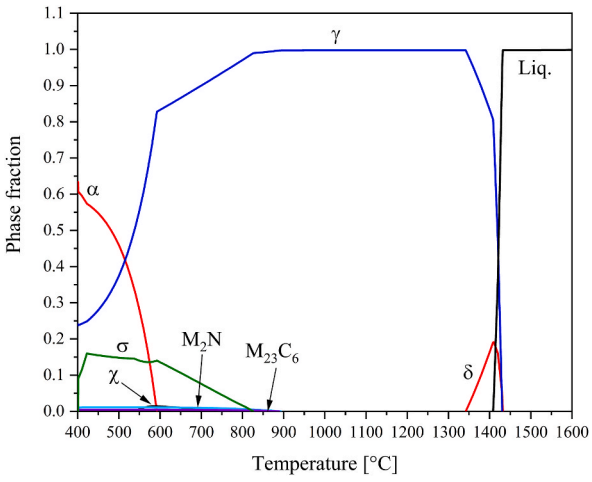

Fig. 19. Sketch of the thermal stability of the unconventional hierarchical microstructure features found in as-built L-PBF austenitic stainless steel.

such as N (or C) migrate to dislocation structures and cause locking of the dislocations [45]. This phenomenon has been reported to occur when pre-deformed austenitic steels are aged in this temperature range [46]. In the range of low treatment temperatures, i.e., 600–700 °C, the dislocation network establishing the cell walls gradually becomes more diffuse. The cell structure dissolves between 800 and 900 °C, consistent with other observations in the literature [3,11,14]. Interestingly, as the cell structures disappear above 800 °C, precipitates appear, that form a pattern reminiscent of the former cell walls. Such precipitation at (former) cell walls is most likely related to the segregation of alloying elements at these locations. The precipitate distribution could maintain some strength through dislocation pinning and in preventing grain/domain boundary migration during prolonged heat treatment. While the cell structure disappears, the domains remain. At higher temperatures, the domain walls appear to develop into straight, well-defined low-angle grain boundaries. The domains largely retain the original size as in the as-built condition, i.e., 3–5 μm. Only for temperatures above 1000 °C limited domain growth is observed, indicating that the domain walls are pinned by precipitates. The strengthening effect of low-angle boundaries separating the domains is not entirely clear; high-angle grain boundaries are anticipated to be more effective barriers, but low-angle boundaries are anticipated to be less mobile as high-angle boundaries.

4.3. Evolution of particle composition and crystallinity

Simultaneously with the dissolution of the dislocation cell wall structure and segregation at cell walls, the particles that formed during L-PBF evolved morphologically, crystallographically and compositionally. The main changes appear after annealing at 700 °C, where small particles of crystalline σ-phase have nucleated adjacent to or onto some of the spherical amorphous silicates. Usually, the precipitation of σ-phase in austenitic stainless steels proceeds slowly [47], but here σ-phase is detected already after only 1 h at 700 °C. Similar observations were reported by Yin et al. who found faster nucleation and growth of σ-phase in L-PBF 316 L as compared to conventionally manufactured steel with and without cold work [11]. The faster nucleation of σ phase in L-PBF is explained by the presence of silicates as heterogeneous nucleation sites in the cell walls, which are enriched in the main alloying elements in σ-phase (Cr and Mo). The shape of the σ-phase precipitates is irregular as compared to the spherical as-built silicates, but this is common for σ-phase in austenite [11,16,45]. In addition to the silicates that formed during L-PBF (with low contents of Mn and Cr), also much smaller, spherical precipitates form, away from the primary silicates. These silicates consist of a significant amount of Si and O and contain more Mn than the silicates present in the as-built condition. These precipitates start to nucleate at an intermediate annealing temperature. Heat treatment at 800 °C leads to a similar response as heat treatment at 700 °C. However, due to faster nucleation and diffusion kinetics at higher temperatures, the σ-phase precipitates are larger. Furthermore, the composition of the σ-phase that formed at 800 °C has a higher Mo content than at 700 °C. This is consistent with CALPHAD modelling in Thermo-Calc, where the equilibrium content of Mo in σ-phase increases with temperature, marked in blue in Fig. 17. Especially at 800 °C, the experimentally determined compositions of σ-phase deviate from the equilibrium composition. This is unusual as the higher temperature should allow the composition to approach equilibrium more efficiently than annealing at 700 °C. σ-phase formation is also the observed mechanism at this temperature for longer treatment times [11].

Interestingly, the primary silicates adjacent to the σ-phase are no longer perfectly spherical, but oval shaped, which could be due to the partial dissolution of the particles or minimization of interfacial energy as the particles are becoming crystalline. Again, small silicates with a relatively high Mn content are formed. While these particles are similar to those at lower temperatures, they tend to contain a higher Mn content as compared to silicate inclusions formed at 700 °C.

σ-Phase is not stable at a temperature above ~830 °C (see ThermoCalc results in Fig. 20), consistent with their absence after annealing at 900 °C.

The primary amorphous silicates are almost entirely dissolved and are replaced by the more Mn-rich silicates that were observed as very small precipitates at lower temperatures. At 900 °C, these Mn-rich silicates have sufficiently favourable conditions to grow at the expense of the primary silicates. These Mn–Si–O particles are crystalline rather than amorphous as observed in the as-built condition

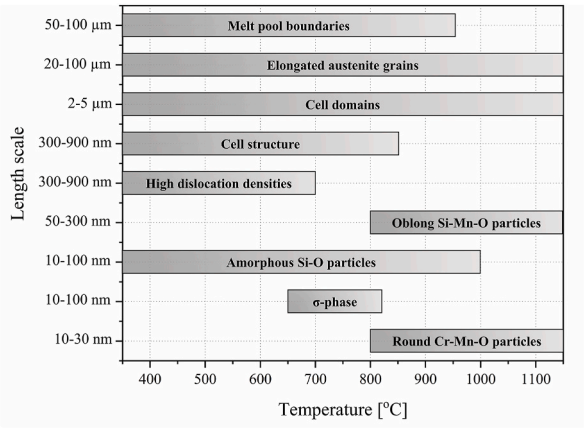

Fig. 20. CALPHAD model of the phase fractions of the phases present in additively manufactured 316 L.

and at lower annealing temperatures. At 900 °C, the Mn-rich silicates are spherical or oval and develop into elongated oblong-shaped large crystalline (>300 nm) particles at 1000 and 1100 °C. The change in shape is ascribed to crystallization and minimization of the interfacial energy between the matrix and particles. Growth of large particles and the disappearance of smaller particles of the same composition is consistent with interfacial energy minimization as a driving force (Ostwald ripening). Apart from the large particles, very small particles containing Cr, Mn and O appear. The high titanium content in some precipitates is likely related to titanium being added to the alloy as stabilization of the austenite to limit the risk of sensitization [48,49].

This systematic investigation into the evolution of the well-known spherical amorphous provides valuable information on not only which phases form but also how these precipitates nucleate and grow. Using carbon extraction replicas enables clearer identification of the chemical composition and crystallography of these fine precipitates due to removal of interference from the matrix austenite phase. This technique appears promising to provide detailed information on the fine precipitation occurring in many additively manufactured metals.

4.4. Implications of microstructure evolution for application of L-PBF austenitic stainless steel

Stress relief (heat) treatment is mandatory for most additively manufactured components to remove the part from the build plate and avoid deformation or, worse, crack formation by the release of accumulated thermal and growth (residual) stresses in the component. The stress relief treatment temperature and time should be chosen carefully, so that sufficient residual stresses from the L-PBF process are redistributed or, better, annihilated, without compromising the integrity of the unconventional microstructural features of the as-built material. In the literature, a wide variety of stress relief temperatures has been applied to L-PBF 316 L, from 470 to 900 °C [39,50–52], regardless of general recommendations to avoid the temperature range ~500–1000 °C to prevent sensitization and associated loss of corrosion properties [53,54]. The risk for sensitization is often mitigated by using a low-carbon austenitic grade as 316 L, where chromium carbide precipitation is only observed after excessively long treatment times (>100 h) in this intermediate temperature range [11,14]. However, while the carbon content in this alloy is kept below 0.03 wt%, the L-PBF 316 L contains around 0.09 wt% nitrogen. This induces a risk of sensitization by chromium nitride formation. Furthermore, choosing a too high stress relief temperature will, as observed in this study, result in a relatively fast formation of σ-phase. Since σ-phase is rich in Cr and Mo, their formation also implies a risk of sensitization and reduced corrosion resistance [55]. In addition, σ-phase in austenitic stainless steel is known to compromise ductility and, in particular, impact toughness [54,56].

The hierarchical as-built microstructure is known to provide excellent mechanical properties with high yield and tensile strengths, while maintaining good ductility [3,57,58]. These properties will change if high temperature treatments are applied, because the main strengthening mechanisms, i.e. dislocation structures, dissolve above 700 °C. However, in certain applications, using these high temperature treatments can be necessary to reduce mechanical anisotropy, which could be undesirable from design perspectives.

5. Conclusions

This study was conducted to gain an understanding of not only the unconventional microstructure formed during L-PBF of austenitic stainless steel, but also how this microstructure evolves as a function of thermal exposure.

- An additional level of the hierarchical microstructure has been characterized in additional detail as the cells are observed to be clustered in domains with a low-angle misorientation to neighbouring domains with negligible misorientation between neighbouring cells, despite a high density of entangled dislocations. The domains are thermally stabilized through the formation of precipitates at the domain boundaries.
- The elongated austenite grains are thermally stable as no abnormal grain growth or recrystallization was observed. The melt pool "boundaries" are more thermally stable than the cell structure.
- The spherical amorphous silicates formed during L-PBF were found to consist mainly of Si and O with varying contents of Mn. These precipitates act as nucleation sites for σ-phase during annealing at intermediate temperatures. At high annealing temperatures, the amorphous silicates are replaced by crystalline oxides. Si–Mn–O particles grow to a large size and form an oblong shape, while Cr–Mn–O particles are round and much smaller.

Author contribution statement

Cecilie V. Funch: Conceived and designed the experiments; Performed the experiments; Analyzed and interpreted the data; Wrote the paper.

Flemming B. Grumsen: Performed the experiments; Analyzed and interpreted the data.

Alice B. da Silva Fanta: Performed the experiments; Contributed reagents, materials, analysis tools or data.

Thomas L. Christiansen; Marcel A.J. Somers: Conceived and designed the experiments; Analyzed and interpreted the data; Wrote the paper.

Data availability statement

Data will be made available on request.

Declaration of competing interest

The authors declare that they have no known competing financial interests or personal relationships that could have appeared to influence the work reported in this paper

Acknowledgements

This study was conducted in connection with the AM-LINE 4.0 project, funded by the Danish Innovation Fund [grant number 7076-00074 B].

References

[1] D. Herzog, V. Seyda, E. Wycisk, C. Emmelmann, Additive manufacturing of metals, Acta Mater. 117 (2016) 371–392, https://doi.org/10.1016/j.actamat.2016.07.019.
[2] T. DebRoy, H.L. Wei, J.S. Zuback, T. Mukherjee, J.W. Elmer, J.O. Milewski, A.M. Beese, A. Wilson-Heid, A. De, W. Zhang, Additive manufacturing of metallic components – process, structure and properties, Prog. Mater. Sci. 92 (2018) 112–224, https://doi.org/10.1016/j.pmatsci.2017.10.001.
[3] Y.M. Wang, T. Voisin, J.T. McKeown, J. Ye, N.P. Calta, Z. Li, Z. Zeng, Y. Zhang, W. Chen, T.T. Roehling, R.T. Ott, M.K. Santala, P.J. Depond, M.J. Matthews, A. V. Hamza, T. Zhu, Additively manufactured hierarchical stainless steels with high strength and ductility, Nat. Mater. 17 (2017) 63–70, https://doi.org/10.1038/NMAT5021.
[4] K.G. Prashanth, J. Eckert, Formation of metastable cellular microstructures in selective laser melted alloys, J. Alloys Compd. 707 (2017) 27–34, https://doi.org/10.1016/j.jallcom.2016.12.209.
[5] Y. Zhong, L. Liu, S. Wikman, D. Cui, Z. Shen, Intragranular cellular segregation network structure strengthening 316L stainless steel prepared by selective laser melting, J. Nucl. Mater. 470 (2016) 170–178, https://doi.org/10.1016/j.jnucmat.2015.12.034.
[6] A.J. Birnbaum, J.C. Steuben, E.J. Barrick, A.P. Iliopoulos, J.G. Michopoulos, Intrinsic strain aging, Σ3 boundaries, and origins of cellular substructure in additively manufactured 316L, Addit. Manuf. 29 (2019), 100784, https://doi.org/10.1016/j.addma.2019.100784.
[7] K. Saeidi, X. Gao, Y. Zhong, Z.J. Shen, Hardened austenite steel with columnar sub-grain structure formed by laser melting, Mater. Sci. Eng. 625 (2015) 221–229, https://doi.org/10.1016/j.msea.2014.12.018.
[8] K. Saeidi, L. Kvetková, F. Lofaj, Z. Shen, Austenitic stainless steel strengthened by the in situ formation of oxide nanoinclusions, RSC Adv. 5 (2015), 20747, https://doi.org/10.1039/c4ra16721j.
[9] N. Chen, G. Ma, W. Zhu, A. Godfrey, Z. Shen, G. Wu, X. Huang, Enhancement of an additive-manufactured austenitic stainless steel by post-manufacture heat-treatment, Mater. Sci. Eng. 759 (2019) 65–69, https://doi.org/10.1016/j.msea.2019.04.111.
[10] K. Saeidi, X. Gao, F. Lofaj, L. Kvetková, Z.J. Shen, Transformation of austenite to duplex austenite-ferrite assembly in annealed stainless steel 316L consolidated by laser melting, J. Alloys Compd. 633 (2015) 463–469, https://doi.org/10.1016/j.jallcom.2015.01.249.
[11] H. Yin, M. Song, P. Deng, L. Li, B.C. Prorok, X. Lou, Thermal stability and microstructural evolution of additively manufactured 316L stainless steel by laser powder bed fusion at 500–800 °C, Addit, Man (Lond.) 41 (2021), 101981, https://doi.org/10.1016/j.addma.2021.101981.
[12] M.S.I.N. Kamariah, W.S.W. Harun, N.Z. Khalil, F. Ahmad, M.H. Ismail, S. Sharif, Effect of heat treatment on mechanical properties and microstructure of selective laser melting 316L stainless steel, IOP Conf. Ser. Mater. Sci. Eng. 257 (2017) 1–11, https://doi.org/10.1088/1757-899X/257/1/012021.
[13] O.O. Salman, C. Gammer, A.K. Chaubey, J. Eckert, S. Scudino, Effect of heat treatment on microstructure and mechanical properties of 316L steel synthesized by selective laser melting, Mater. Sci. Eng. 748 (2019) 205–212, https://doi.org/10.1016/j.msea.2019.01.110.
[14] P. Deng, H. Yin, M. Song, D. Li, Y. Zheng, B.C. Prorok, X. Lou, On the thermal stability of dislocation cellular structures in additively manufactured austenitic stainless steels: roles of heavy element segregation and stacking fault energy, Jom 72 (2020) 4232–4243, https://doi.org/10.1007/s11837-020-04427-7.
[15] C. Man, Z. Duan, Z. Cui, C. Dong, D. Kong, T. Liu, S. Chen, X. Wang, The effect of sub-grain structure on intergranular corrosion of 316L stainless steel fabricated via selective laser melting, Mater. Lett. 243 (2019) 157–160, https://doi.org/10.1016/j.matlet.2019.02.047.
[16] T. Kurzynowski, K. Gruber, W. Stopyra, B. Kuźnicka, E. Chlebus, Correlation between process parameters, microstructure and properties of 316L stainless steel processed by selective laser melting, Mater. Sci. Eng. 718 (2018) 64–73, https://doi.org/10.1016/j.msea.2018.01.103.
[17] B. Blinn, M. Klein, C. Gläßner, M. Smaga, J.C. Aurich, T. Beck, An investigation of the microstructure and fatigue behavior of additively manufactured AISI 316L stainless steel with regard to the influence of heat treatment, Metals 8 (2018) 220, https://doi.org/10.3390/met8040220.
[18] R.W. Fonda, D.J. Rowenhorst, C.R. Feng, A.J. Levinson, K.E. Knipling, S. Olig, A. Ntiros, B. Stiles, R. Rayne, The effects of post-processing in additively manufactured 316L stainless steels, Metall. Mater. Trans. A Phys. Metall. Mater. Sci. 51 (2020) 6560–6573, https://doi.org/10.1007/s11661-020-06039-x.
[19] C. Zhou, S. Hu, Q. Shi, H. Tao, Y. Song, J. Zheng, P. Xu, L. Zhang, Improvement of corrosion resistance of SS316L manufactured by selective laser melting through subcritical annealing, Corrosion Sci. 164 (2020), 108353, https://doi.org/10.1016/j.corsci.2019.108353.
[20] F. Yan, W. Xiong, E. Faierson, G.B. Olson, Characterization of nano-scale oxides in austenitic stainless steel processed by powder bed fusion, Scripta Mater. 155 (2018) 104–108, https://doi.org/10.1016/j.scriptamat.2018.06.011.
[21] C. V Funch, K. Somlo, T.L. Christiansen, M.A.J. Somers, Thermochemical post-processing of additively manufactured austenitic stainless steel, Surf. Coat. Technol. 441 (2022), 128495, https://doi.org/10.1016/j.surfcoat.2022.128495.
[22] C.V. Funch, T.L. Christiansen, M.A.J. Somers, Effect of edge print parameters on microstructure and high temperature solution nitriding response of additively manufactured austenitic stainless steel, Surf. Coating. Technol. 403 (2020), 126385, https://doi.org/10.1016/j.surfcoat.2020.126385.
[23] M.O. Speidel, Nitrogen containing austenitic stainless steels, Mater. Werkst. 37 (2006) 875–880, https://doi.org/10.1002/mawe.200600068.
[24] N. Yang, J. Yee, B. Zheng, K. Gaiser, T. Reynolds, L. Clemon, W.Y. Lu, J.M. Schoenung, E.J. Lavernia, Process-structure-property relationships for 316L stainless steel fabricated by additive manufacturing and its implication for component engineering, J. Therm. Spray Technol. 26 (2017) 610–626, https://doi.org/10.1007/s11666-016-0480-y.
[25] M.L. Montero Sistiaga, S. Nardone, C. Hautfenne, J. Van Humbeeck, Effect of heat treatment of 316L stainless steel produced by selective laser melting (SLM), 27th Annu. Int. Solid Free. Fabr. Symp. - An Addit. Manuf. Conf. Solid Free. Fabr. Symp. (2016) 558–565.
[26] J.C. Lippold, D.J. Kotecki, Austenitic stainless steels, in: Weld. Metall. Weldability, Stainl. Steels, 2005, pp. 141–163, https://doi.org/10.1016/B978-0-12-397046-6.00008-3.
[27] T. Ronneberg, C.M. Davies, P.A. Hooper, Revealing relationships between porosity, microstructure and mechanical properties of laser powder bed fusion 316L stainless steel through heat treatment, Mater. Des. 189 (2020), 108481, https://doi.org/10.1016/j.matdes.2020.108481.
[28] R. Casati, J. Lemke, M. Vedani, Microstructure and fracture behavior of 316L austenitic stainless steel produced by selective laser melting, J. Mater. Sci. Technol. 32 (2016) 738–744, https://doi.org/10.1016/j.jmst.2016.06.016.
[29] W.M. Tucho, V.H. Lysne, H. Austbø, A. Sjolyst-Kverneland, V. Hansen, Investigation of effects of process parameters on microstructure and hardness of SLM manufactured SS316L, J. Alloys Compd. 740 (2018) 910–925, https://doi.org/10.1016/j.jallcom.2018.01.098.
[30] R. Sedláček, W. Blum, J. Kratochvíl, S. Forest, Subgrain formation during deformation: physical origin and consequences, Metall. Mater. Trans. 32A (2001) 1–9, papers://82d09eba-ea7e-42aa-9e88-31cb27a3a70e/Paper/p.310.
[31] S. Kurian, R. Mirzaeifar, Deformation mechanisms of the subgranular cellular structures in selective laser melted 316L stainless steel, Mech. Mater. 148 (2020), https://doi.org/10.1016/j.mechmat.2020.103478.

[32] A. Yadollahi, N. Shamsaei, S.M. Thompson, D.W. Seely, Effects of process time interval and heat treatment on the mechanical and microstructural properties of direct laser deposited 316L stainless steel, Mater. Sci. Eng. 644 (2015) 171–183, https://doi.org/10.1016/j.msea.2015.07.056.
[33] T. Voisin, J.-B. Forien, A. Perron, S. Aubry, N. Bertin, A. Samanta, A. Baker, Y.M. Wang, New insights on cellular structures strengthening mechanisms and thermal stability of an austenitic stainless steel fabricated by laser powder-bed-fusion, Acta Mater. 203 (2021), 116476, https://doi.org/10.1016/j.actamat.2020.11.018.
[34] V.D. Manvatkar, A.A. Gokhale, G. Jagan Reddy, A. Venkataramana, A. De, Estimation of melt pool dimensions, thermal cycle, and hardness distribution in the laser-engineered net shaping process of austenitic stainless steel, Metall. Mater. Trans. A Phys. Metall. Mater. Sci. 42 (2011) 4080–4087, https://doi.org/10.1007/s11661-011-0787-8.
[35] S. Dehgahi, M. Sanjari, M.H. Ghoncheh, B.S. Amirkhiz, M. Mohammadi, Concurrent improvement of strength and ductility in heat-treated C300 maraging steels produced by laser powder bed fusion technique, Addit. Manuf. 39 (2021), 101847, https://doi.org/10.1016/j.addma.2021.101847.
[36] J.R. Trelewicz, G.P. Halada, O.K. Donaldson, G. Manogharan, Microstructure and corrosion resistance of laser additively manufactured 316L stainless steel, J. Occup. Med. 68 (2016) 850–859, https://doi.org/10.1007/s11837-016-1822-4.
[37] J.W. Elmer, S.M. Allen, T.W. Eagar, Microstructural development during solidification of stainless steel alloys, Metall. Trans. A 20 (1989) 2117–2131, https://doi.org/10.1007/BF02650298.
[38] M. Zietala, T. Durejko, M. Polanski, I. Kunce, T. Plocinski, W. Zielinski, M. Lazinska, W. Stepniowski, T. Czujko, K.J. Kurzydlowski, Z. Bojar, The microstructure, mechanical properties and corrosion resistance of 316L stainless steel fabricated using laser engineered net shaping, Mater. Sci. Eng. 677 (2016) 1–10, https://doi.org/10.1016/j.msea.2016.09.028.
[39] M. Ma, Z. Wang, X. Zeng, A comparison on metallurgical behaviors of 316L stainless steel by selective laser melting and laser cladding deposition, Mater. Sci. Eng. 685 (2017) 265–273, https://doi.org/10.1016/j.msea.2016.12.112.
[40] P. Krakhmalev, G. Fredriksson, K. Svensson, I. Yadroitsev, I. Yadroitsava, M. Thuvander, R. Peng, Microstructure, solidification texture, and thermal stability of 316L stainless steel manufactured by laser powder bed fusion, Metals 8 (2018), https://doi.org/10.3390/met8080643.
[41] S. Bahl, S. Mishra, K.U. Yazar, I.R. Kola, K. Chatterjee, S. Suwas, Non-equilibrium microstructure, crystallographic texture and morphological texture synergistically result in unusual mechanical properties of 3D printed 316L stainless steel, Addit. Manuf. 28 (2019) 65–77, https://doi.org/10.1016/j.addma.2019.04.016.
[42] P. Deng, M. Karadge, R.B. Rebak, V.K. Gupta, B.C. Prorok, X. Lou, The origin and formation of oxygen inclusions in austenitic stainless steels manufactured by laser powder bed fusion, Addit. Manuf. 35 (2020), 101334, https://doi.org/10.1016/j.addma.2020.101334.
[43] M.V. Staritsyn, P.A. Kuznetsov, S.N. Petrov, M.S. Mikhailov, Composite structure as a strengthening factor of stainless austenitic chromium–nickel additive steel, Phys. Met. Metallogr. 121 (2020) 337–343, https://doi.org/10.1134/S0031918X20040146.
[44] E. Werner, Solid solution and grain size hardening of nitrogen-alloyed austenitic steels, Mater. Sci. Eng. 101 (1988) 93–98, https://doi.org/10.1016/0921-5093(88)90054-8.
[45] C. Yu, Y. Zhong, P. Zhang, Z. Zhang, C. Zhao, Z. Zhang, Z. Shen, W. Liu, Effect of build direction on fatigue performance of L-PBF 316L stainless steel, Acta Metall. Sin. (English Lett. 33 (2020) 539–550, https://doi.org/10.1007/s40195-019-00983-3.
[46] S.H. Lee, J.Y. Choi, W.J. Nam, Hardening behavior of a 304 stainless steel containing deformation-induced martensite during static strain aging, Mater. Trans. 50 (2009) 926–929, https://doi.org/10.2320/matertrans.MRP2008416.
[47] D.M.E. Villanueva, F.C.P. Junior, R.L. Plaut, A.F. Padilha, Comparative study on sigma phase precipitation of three types of stainless steels: austenitic, superferritic and duplex, Mater. Sci. Technol. 22 (2006) 1098–1104, https://doi.org/10.1179/174328406X109230.
[48] E.H. Valente, T.L. Christiansen, M.A.J. Somers, The effect of heat treatment and surface hardening of 3d printed austenitic stainless steel aisi316l on corrosion and wear properties, ESSC DUPLEX 2019 - 10th, Eur. Stainl. Steel Conf. - Sci. Mark. 6th Eur. Duplex Stainl. Steel Conf. Exhib. (2019) 42–51.
[49] M.F. McGuire, Austenitic stainless steels, in: Encycl. Mater. Sci. Technol., 2011, pp. 406–411.
[50] A.F. Padilha, P.R. Rios, Decomposition of austenite in austenitic stainless steels, ISIJ Int. 42 (2002) 325–337.
[51] X. Lou, M. Song, P.W. Emigh, M.A. Othon, P.L. Andresen, On the stress corrosion crack growth behaviour in high temperature water of 316L stainless steel made by laser powder bed fusion additive manufacturing, Corrosion Sci. 128 (2017) 140–153, https://doi.org/10.1016/j.corsci.2017.09.017.
[52] B. Blinn, F. Krebs, M. Ley, R. Teutsch, T. Beck, Determination of the influence of a stress-relief heat treatment and additively manufactured surface on the fatigue behavior of selectively laser melted AISI 316L by using efficient short-time procedures, Int. J. Fatig. 131 (2020), 105301, https://doi.org/10.1016/j.ijfatigue.2019.105301.
[53] W.J. Lai, A. Ojha, Z. Li, C. Engler-Pinto, X. Su, Effect of residual stress on fatigue strength of 316L stainless steel produced by laser powder bed fusion process, Prog. Addit. Manuf. 6 (2021) 375–383, https://doi.org/10.1007/s40964-021-00164-8.
[54] A.F. Padilha, R.L. Plaut, Stainless steel heat treatment, in: Steel Heat Treat. Handb., Taylor & Francis Ltd, London, 2006, pp. 695–735.
[55] J.D. Fritz, Heat treating of austenitic and duplex stainless steels, in: J.L. Dossett, G.E. Totten (Eds.), Heat Treat. Irons Steels, 4D, ASM Handb., ASM international, 2014, pp. 370–381.
[56] O. Conejero, M. Palacios, S. Rivera, Premature corrosion failure of a 316L stainless steel plate due to the presence of sigma phase, Eng. Fail. Anal. 16 (2009) 699–704, https://doi.org/10.1016/j.engfailanal.2008.06.022.
[57] X. Chen, J. Li, X. Cheng, B. He, H. Wang, Z. Huang, Microstructure and mechanical properties of the austenitic stainless steel 316L fabricated by gas metal arc additive manufacturing, Mater. Sci. Eng. 703 (2017) 567–577, https://doi.org/10.1016/j.msea.2017.05.024.
[58] P. Bajaj, A. Hariharan, A. Kini, P. Kürnsteiner, D. Raabe, E.A. Jägle, Steels in additive manufacturing: a review of their microstructure and properties, Mater. Sci. Eng. 772 (2020), 138633, https://doi.org/10.1016/j.msea.2019.138633.